nature astronomy

Article

https://doi.org/10.1038/s41550-024-02305-9

Ionospheric irregularities at Jupiter observed by JWST

Received: 18 May 2023

Accepted: 29 May 2024

Published online: 21 June 2024

Check for updates

Henrik Melin[1,16] ✉, J. O'Donoghue[2,3], L. Moore[4,5], T. S. Stallard[4], L. N. Fletcher[6], M. T. Roman[6], J. Harkett[6], O. R. T. King[6], E. M. Thomas[6], R. Wang[6], P. I. Tiranti[6], K. L. Knowles[1], I. de Pater[7], T. Fouchet[8], P. H. Fry[9], M. H. Wong[7], B. J. Holler[10], R. Hueso[11], M. K. James[6], G. S. Orton[12], A. Mura[13], A. Sánchez-Lavega[11], E. Lellouch[8], K. de Kleer[14] & M. R. Showalter[15]

Jupiter's upper atmosphere is composed of a neutral thermosphere and charged ionosphere. In the latter, the dominant molecular ion H_3^+ emits in the near-infrared, allowing for the remote exploration of the physical properties of the upper atmosphere. However, the Jovian low-latitude ionosphere remains largely unexplored because H_3^+ emissions from this region are faint and spectrally entangled with bright neutral species, such as CH_4. Here, we present James Webb Space Telescope H_3^+ observations of Jupiter's low-latitude ionosphere in the region of the Great Red Spot, showing unexpected small-scale intensity features such as arcs, bands and spots. Our observations may imply that the low-latitude ionosphere of Jupiter is strongly coupled to the lower atmosphere via gravity waves that superimpose to produce this complex and intricate morphology.

The extent to which the non-auroral upper atmosphere of Jupiter is coupled to the convective-radiative atmosphere below and to the magnetosphere above is largely unknown because ground-based observations do not offer the sensitivity required to investigate this. The James Webb Space Telescope (JWST) performed observations of Jupiter's Great Red Spot (GRS) with the NIRSpec Integral Field Unit (IFU) on 27 July 2022 as part of the Early Release Science programme (ERS #1373 (ref. 1)). The F290LP/G395H filter/grating produced a spectrum between 2.87 and 5.27 μm with a spectral resolving power of $R = 2{,}700$. In this Article, we use the short-wavelength (NRS1) detector only, covering 2.85–4.01 μm. The observational setup is shown in Fig. 1a, with JWST acquiring six IFU spectral cubes over a period of 53 min, each with an effective integration time of 5.4 min. The observational details are summarized in Table 1. The NIRSpec IFU has 30 × 30 spaxels, each measuring 0.1″ × 0.1″, producing a spatial resolution of ~300 km per spaxel on the planet. This wavelength region contains emissions from the molecular ion H_3^+, a dominant ion in the charged-particle ionosphere, along with H^+, situated at altitudes >300 km above the cloud deck[2]. This ion is produced by both electron-impact ionization about the magnetic poles and solar photo-ionization on the dayside of the planet, which dominates as a production mechanism in the low-latitude ionosphere[3]. In the absence of dynamic interactions with the atmosphere and magnetosphere, the low-latitude ionosphere may be expected to emit in a relatively uniform manner, given that the incoming solar flux at these heliospheric distances will be constant across the disk at any given moment, with a peak production of H_3^+ occurring at the subsolar point. At low latitudes, the H_3^+ emissions are roughly ten times weaker than the auroral region[4] and are blended with strong solar excited non-local thermodynamic

[1]Northumbria University, Newcastle upon Tyne, UK. [2]Department of Meteorology, University of Reading, Reading, UK. [3]JAXA Institute of Space and Astronautical Science, Sagamihara, Japan. [4]Department of Astronomy, Boston University, Boston, MA, USA. [5]Center for Space Physics, Boston University, Boston, MA, USA. [6]University of Leicester, Leicester, UK. [7]University of California, Berkeley, CA, USA. [8]Observatoire de Paris, Meudon, France. [9]University of Wisconsin, Madison, WI, USA. [10]Space Telescope Science Institute, Baltimore, MD, USA. [11]Universidad del País Vasco, UPV/EHU, Bilbao, Spain. [12]Jet Propulsion Laboratory, California Institute of Technology, Pasadena, CA, USA. [13]INAF-Istituto di Astrofisica e Planetologia Spaziali, Rome, Italy. [14]California Institute of Technology, Pasadena, CA, USA. [15]SETI Institute, Mountain View, CA, USA. [16]Present address: University of Leicester, Leicester, UK.
✉e-mail: henrik.melin@northumbria.ac.uk

https://doi.org/10.1038/s41550-024-02305-9

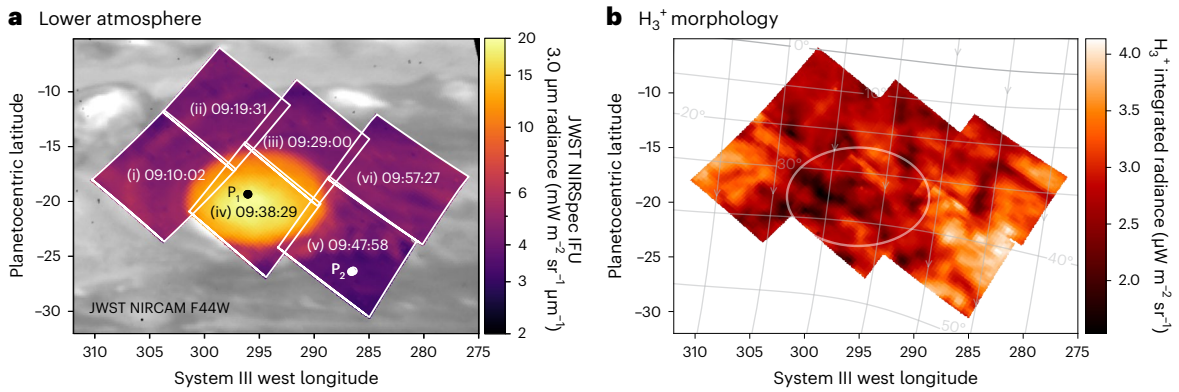

Fig. 1 | JWST observations of Jupiter's GRS. a, The JWST NIRSpec IFU mosaic sequence used to capture Jupiter's GRS area on 27 July 2022, shown together with the 3 μm aerosol scattering from the upper troposphere. The times are the midpoint of each observation, and the background image is a JWST Near Infrared Camera (NIRCAM) observation from 27 July 2022 20:27:10 using the F440W filter. Figure 2 shows spectra at points P_1 and P_2. **b**, The integrated H_3^+ radiance extracted from the NIRSpec observations. The horizontal grey lines show the magnetic dip angle, and the vertical grey lines shows the orientation of the magnetic field lines as mapped above the surface, spaced by 10° longitude[9]. The oval shows the location of the GRS.

equilibrium (LTE) methane emissions[5]. This makes any observations of this region from the ground challenging[6] and therefore a suitable target for JWST. The integrated ionospheric H_3^+ emissions are shown in Fig. 1b, and the analysis procedure is outlined below.

In Fig. 1a, two points are indicated: P_1 at the GRS and P_2 away from it. The NIRSpec spectra for these points are shown in Fig. 2b, together with a model H_3^+ spectrum in Fig. 2a. The observed radiances are clearly much higher at the GRS than away from it, showing an enhancement in the reflective aerosols in the upper troposphere and lower stratosphere at the GRS, extending up to 40–50 mbar (ref. 7). This figure also illustrates the challenge in extracting the H_3^+ spectrum from this region, which is rich in spectral features: the H_3^+ signal is very weak compared to bright structures generated in the lower part of the atmosphere, with H_3^+ peaking at ~1 mW m^{-2} sr^{-1} μm^{-1} and the peak radiance at 3.9 μm reaching up to ~20 mW m^{-2} sr^{-1} μm^{-1} where the H_3^+ $Q(1, 0^-)$ line is situated. However, between 3.2 and 3.6 μm, deep CH_4 absorbs most of the incoming sunlight, rendering this region spectrally dark, and the discrete H_3^+ emission can be readily extracted after the subtraction of the high-altitude solar-pumped non-LTE CH_4 spectrum. This process is repeated for each spaxel and is illustrated in Fig. 3 and expanded upon in the Methods. Note that the strong H_3^+ line at ~3.46 μm is omitted in this analysis because it is blended with a bright feature produced by the absence of methane opacity in the lower atmosphere[8], which is not readily modelled. The spectral regions used in this study are shaded grey in Fig. 2, containing 21 H_3^+ emission lines (Supplementary Table 1). Overall, the solar-pumped CH_4 emissions do not show any substantial small-scale variation across the field of view (Supplementary Fig. 1).

The H_3^+ emissions extracted from the NIRSpec data can be seen in Fig. 1b, together with the magnetic field topology across this region[9]. A striking result of JWST observations that was never seen in previous ground-based images[4] is the presence of intricate small-scale structures. These are visible in this small patch on the planet, covering only 37° longitude and 27° latitude. In fact, ground-based observations need to average over several nights to bring out low-latitude features, preventing us from seeing the instantaneous ionospheric structure, which now reveals its complex morphology. There are discrete features that form bands and arcs ~1,000 km wide and up to ~6,000 km long. On average, H_3^+ is relatively dark inside the GRS, with two bright regions to the northwest and southeast of it. Across the field of view, the integrated radiance varies by up to a factor 4. The intensity of H_3^+ is governed both by ion density and by the temperature of the upper atmosphere, with which the ion thermalizes. Via H_3^+ spectral retrievals, these two parameters can be disentangled and the driver of the ionospheric emission features can be determined. The extracted

Table 1 | Summary of the JWST NIRSpec IFU observations

Nbr	Date start (UTC)	Time end	Time mid	Lon	Lat	LT (h)
1	27 July 2022 09:07:15	09:12:48	09:10:02	303.8	−17.7	11.0
2	27 July 2022 09:16:44	09:22:17	09:19:31	298.1	−11.6	11.8
3	27 July 2022 09:26:13	09:31:46	09:29:00	290.8	−14.6	12.7
4	27 July 2022 09:35:42	09:41:15	09:38:29	295.6	−20.7	12.7
5	27 July 2022 09:45:11	09:50:44	09:47:58	287.1	−24.1	13.7
6	27 July 2022 09:54:40	10:00:13	09:57:27	282.5	−17.9	14.4

Tile acquisition times at Jupiter's GRS and the tile centre planetocentric latitude (Lat) and System III west longitude (Lon), as well as the local time (LT). The observing sequence is shown in Fig. 1.

spectra for each spaxel (for example, Fig. 3c) are fitted using the open source H_3^+ Python package h3ppy, and the results of these retrievals are shown in Fig. 4. The median temperature of all spaxels is 713 ± 20 K, with a median density of 4.5 ± 0.4 × 10^{15} m^{-2}, broadly consistent with previous studies[10,11].

In Fig. 4, the oval indicates the location of the GRS (from Fig. 1), and the contours show a Gaussian smoothing with a width of 2° longitude and latitude of each fitted parameter, showing the broad-scale structure present in the data. The temperature distribution in Fig. 4a shows higher temperature toward higher latitudes, and three regions appear hotter, with a median temperature of 738 K: (1) at the centre of the GRS and (2) northwest and (3) southeast of it. Northwest of the GRS, the troposphere is extremely turbulent[12] and could be a source of gravity waves. The elevated temperatures at the GRS have larger uncertainties associated with them due to the elevated background emissions (Fig. 4c), but this could be related to an increased homopause altitude above the GRS, which destroys colder H_3^+ at low altitudes via charge exchange, producing column observations of high temperatures and low densities, matching what is seen in Fig. 4. The higher noise levels observed in the GRS might be associated with the presence of elevated hazes that increase the brightness of the GRS at 3.3–3.6 μm. The H_3^+ column-density retrievals in Fig. 4b show patchy structures that are largely mirrored in the integrated radiance (Fig. 1b). Next, we quantitatively investigate the drivers of the discrete H_3^+ radiance features.

https://doi.org/10.1038/s41550-024-02305-9

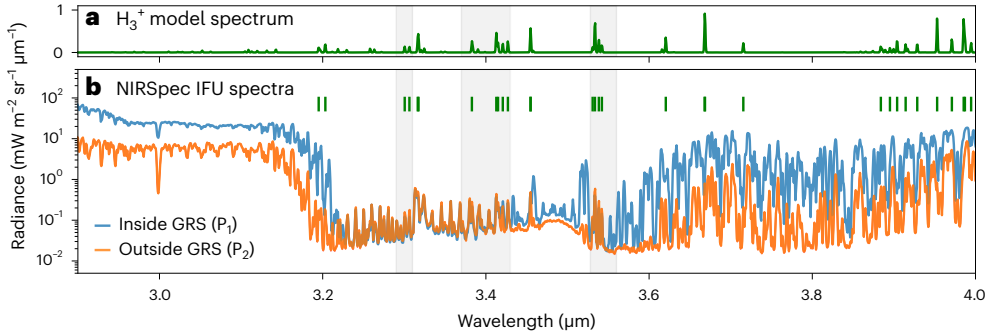

Fig. 2 | JWST NIRSpec Jupiter spectra. a, A model H_3^+ spectrum generated with values consistent with low-latitude emissions (T = 700 K and $N = 5 \times 10^{15}$ m^{-2}). **b**, The NIRSpec IFU F290LP/G395H NRS1 spectra from individual spaxel points P_1 and P_2 shown in Fig. 1, from inside and outside the GRS. The vertical green lines indicate the locations of the brightest H_3^+ lines. The grey shaded area shows the wavelength region considered for this analysis, from which the H_3^+ spectrum is extracted.

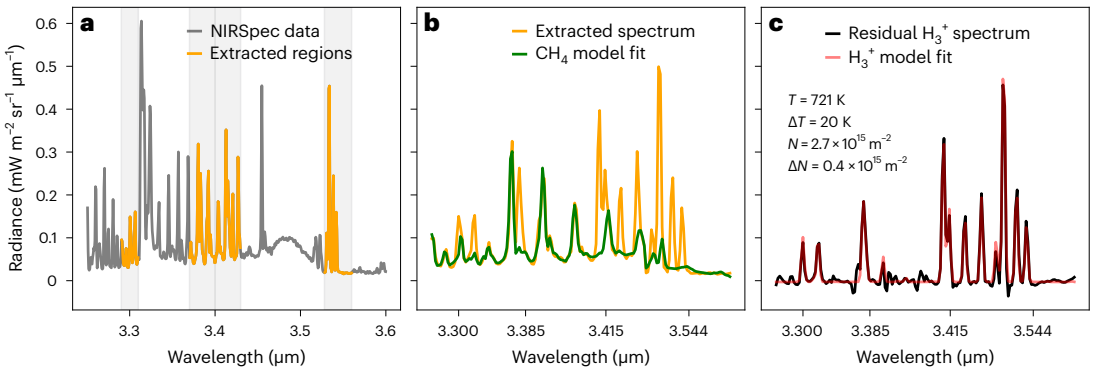

Fig. 3 | H_3^+ extraction procedure. The analysis sequence applied to retrieve H_3^+ model fits to the NIRSpec IFU data. **a**, The spectrum from point P_2 in Fig. 1, from which regions with bright H_3^+ emission lines are extracted. **b**, A CH_4 model is fitted to the extracted spectrum. **c**, Once the CH_4 model is subtracted from the data, isolating the H_3^+ emission lines, the spectrum can be fitted using the Python package h3ppy to retrieve the temperature of the upper atmosphere and ionospheric H_3^+ density.

From the set of NIRSpec observations presented here, mosaic tile (vi) (Fig. 1) contains the clearest (dark) banded structures and is located away from the region with large errors at the centre of the GRS and regions of localized heating. To investigate whether these are produced by reduced temperatures or lower H_3^+ densities, the relationship between these parameters and the integrated H_3^+ radiance are plotted in Fig. 5. A third-order polynomial is fitted to each correlation (black line), with the shaded region showing the extent of the median uncertainty. The relationship between temperature and radiance in Fig. 5b shows that the temperatures are not strongly correlated with the observed H_3^+ radiance, having a Pearson correlation coefficient of 0.15. However, Fig. 5c shows that as the radiance increases, the column density also increases, well outside the density uncertainties, with a correlation coefficient of 0.66. This shows that the observed changes in the H_3^+ radiance is driven primarily by the H_3^+ column density. The correlation relations for the other six mosaic tiles are shown in Supplementary Fig. 2. The Pearson correlation coefficients indicate that the radiance is better correlated with density than the temperature for all but one tile (tile (iii)). This may suggest that although the radiance is generally driven by density, there are small areas where the temperature is a significant driver, perhaps driven by gravity-wave heating[13].

Figure 5 also shows that higher temperatures are generally associated with lower column densities. This anticorrelation is well established and expected (for example, refs. 14,15) and is produced by the fact that the intensity of H_3^+ emissions is driven exponentially by temperature and linearly by density[16], so they are intrinsically anticorrelated. In general, the spatial differences in temperature and density can be trusted if the differences are larger than the derived uncertainties[14], which is not the case for temperatures in Fig. 5b but is the case for densities in Fig. 5c.

In Fig. 4b, the H_3^+ column densities vary by a factor of ~4. In the polar region, the column densities are higher by a factor of ~10, but the column-density variability across the H_3^+ aurorae varies by similar factors[17]. The H_3^+ density variations at high latitudes are related to the discrete auroral field-aligned currents generating vast amounts of H_3^+ via impact ionization. Such large density gradients are a surprise at low latitudes, however, where ion production is dominated by the smoothly varying incident solar flux. High-altitude in situ Juno plasma observations have also suggested that there are significant fluctuations in the H_3^+ density at low latitudes[18], which may be related to the density variations seen here.

The results of this study form the starting point for understanding the short-term and small-scale drivers of Jupiter's low-latitude ionosphere. At Earth, the low-latitude ionosphere is dynamic and rich in features, dominated by electrodynamics[19]. Neutral winds play an important role in the behaviour of this region, carrying the ionospheric plasma with them away from the subsolar point. This generates a strong duskward electric field (**E**), known as the equatorial electrojet. Close to the equator, the magnetic field (**B**) runs parallel to the surface and the magnetic field-line dip angle is zero, also called the magnetic dip equator. At this location, the **E** × **B** force moves ions up in altitude, generating the 'plasma fountain', producing a depletion of plasma at the magnetic dip equator and enhancements in plasma density at either side of it as the plasma diffuses back down due to gravity, known as the equatorial ionization anomaly (EIA). The magnetic field of Jupiter has a magnetic field polarity opposite that of the Earth, reversing the direction of **B** at the equator. This also likely reverses the equatorial

https://doi.org/10.1038/s41550-024-02305-9

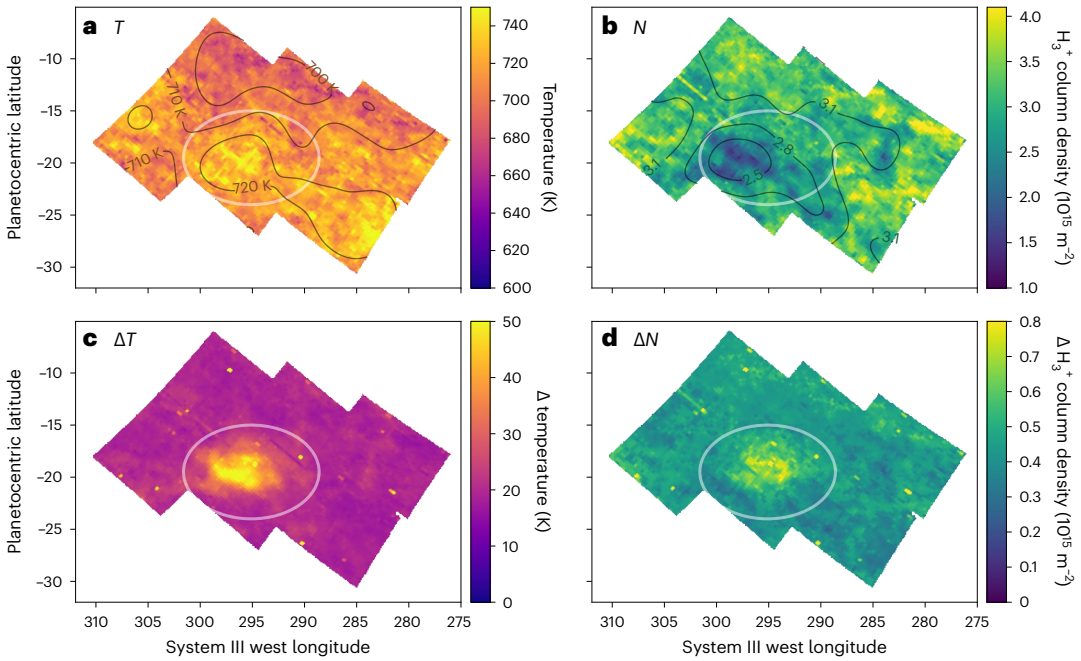

Fig. 4 | Temperature and H_3^+ ion density retrievals. The physical properties of the ionosphere >300 km (ref. 2) above the Great Red Spot area. **a**, the temperature, *T*, of the upper atmosphere, **b**, H_3^+ column integrated density, *N*, **c**, the uncertainty on the retrieved temperature, Δ*T*, **d**, the uncertainty on the retrieved H_3^+ column integrated densities, Δ*N*. **a** and **b** also show contours of the smoothed parameters to reveal broader-scale structures.

electrojet to run dawnward, still resulting in an Earth-like upward **E** × **B** force, producing a plasma fountain, removing H_3^+ ions from the magnetic dip equator. However, our observations show no clear decrease in the H_3^+ density close to the dip equator, nor any evidence for EIAs (Fig. 4b and Supplementary Fig. 3).

Another important driver of ionospheric density perturbations at Earth are gravity waves, which produce travelling ionospheric disturbances (TIDs), where a single travelling wave produces ordered density perturbations in the ionosphere[19]. Above Jupiter's GRS, the ionosphere is likely subject to a complex barrage of upward travelling gravity waves originating from different tropospheric storms[20–22]. This process might explain the complex structures see in Fig. 1b—the superposition of multiple gravity waves changing the H_3^+ density of the ionosphere—and would also explain the arc-like structures seen in the data. For example, the right-angled feature in mosaic tile (vi) could be the result of two perpendicular waves.

A further process that shapes the ionosphere of the Earth at lower latitudes is the propagation of Rayleigh–Taylor instabilities, especially in the post-dusk sector[23]. This process is capable of generating extended features and requires a trigger, such as the removal of the low-altitude ionosphere after dusk or a density fluctuation caused by gravity waves. However, the main H_3^+ density peak at Jupiter is in photochemical equilibrium[24], which will act to limit the development of Rayleigh–Taylor instabilities on the dayside; the relatively short lifetime of H_3^+ means that these cannot be propagated effectively. Therefore, we suggest that TIDs generated by gravity waves are the most likely mechanism responsible for the small-scale features seen in the JWST data.

At Earth, another source of ionospheric irregularities is meteoritic seeding of the upper atmosphere that produces vertical stratification of the ionosphere, known as sporadic E layers, which generates localized increases in the ionospheric density[19]. Jupiter's large mass makes these impacts more common than at the Earth and could therefore be an important contributor to shaping the ionospheric structure, manifesting as H_3^+ density perturbations close to the homopause[25]. The meteoritic ions (Mg^+ and Fe^+) are long lived, with lifetimes of ~300 Jovian rotations; the sporadic layers can also be shaped by gravity waves, and the spatial variability of electron density can significantly alter the lifetimes of H_3^+, shaping the observed densities.

Gravity waves in Jupiter's atmosphere, analogous to TIDs at the Earth, have been modelled[21], showing that they can produce H_3^+ density variations of over an order of magnitude, as well as much smaller perturbations in temperature, up to ~30 K. Because the temperature uncertainties in Fig. 4c are of a similar magnitude, we expect to resolve gravity-wave perturbations only in the H_3^+ column density and not in temperature. The dominant ions in the ionosphere of Jupiter are H^+ and H_3^+, with lifetimes of ~1 Jovian day and ~1,000 s, respectively, at ~300 km (ref. 21). For waves with periods close to the H_3^+ lifetime, only very small H_3^+ density perturbations are expected; but for longer waves with periods closer to the H^+ lifetime, significant H_3^+ variations are predicted. This is because the chemical reactions that govern H_3^+ (that is, production and destruction) occur on much shorter time scales, which means that H_3^+ remains in chemical equilibrium along the wave, so the H_3^+ radiance features are a result of the gravity-wave-induced density perturbations in the H_2 source population. The gravity waves seen in the Galileo entry probe thermal profile[26] are predicted to generate H_3^+ density variations of 5% to 23%, whereas here we see variations of up to a factor of ~4 (for example, see Fig. 5c). Note, however, that the modelled H_3^+ density variations are highly dependent on the wave parameters used, and they do not consider the superposition of multiple gravity waves.

The temporally averaged view of Jupiter's ionosphere produced by adding almost 50 nights of observations[4] showed that the intensity of H_3^+ is strongly linked to the topology of the magnetic field, suggesting that electrodynamic processes shape the structure of Jupiter's low-latitude ionosphere. In stark contrast, the JWST observations presented here suggest that the instantaneous structure of the ionosphere is largely driven by wave dynamics. The equator-ward edge of IFU mosaic tile (ii) reaches the magnetic dip equator (Fig. 1b), but there is no H_3^+ density decrease present to suggest the existence of a plasma fountain or an EIA (Fig. 4 and Supplementary Fig. 3). This is not, however, inconsistent with the electrodynamics revealed by the long-term study. Wave dynamics must govern the short-term behaviour of the low-latitude ionosphere, and only when these are averaged out

https://doi.org/10.1038/s41550-024-02305-9

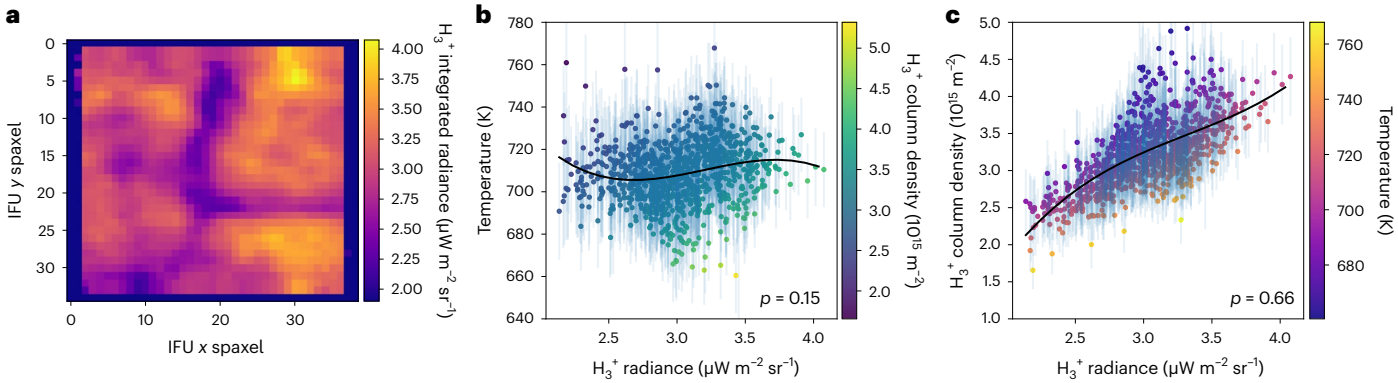

Fig. 5 | Drivers of H_3^+ radiances. a, The integrated H_3^+ radiance for NIRSpec IFU mosaic tile (vi) (Fig. 1). **b**,**c**, Correlation between temperature and radiance (**b**) and column-integrated H_3^+ density and radiance (**c**). The black line shows the third-order polynomial fit to the data, and *p* indicates the Pearson correlation coefficient.

over longer time scales can we reveal features associated with electrodynamics. In other words, in the low-latitude ionosphere of Jupiter, wave dynamics appear to dominate over electrodynamics in the short term, at least in the GRS region. The opposite is true at Earth[19]. Additionally, Jupiter's low-latitude ionosphere has long been considered quite bland[24], especially when contrasted to the dynamic auroral zones. The observations presented here show that this is far from true, and there is a richness in features that have never been seen before.

Although solar photo-ionization is expected to dominate the production of H_3^+ at low latitudes[3], there has been speculation that particle precipitation could also occur in this region[27]. An increase in particle impact ionization would serve to increase the observed H_3^+ density, due to increased ion production. However, the very complex small-scale pattern seen in Fig. 1b would imply an equally complex set of field-aligned currents across this small region, and there is hitherto no evidence of such currents away from the auroral region.

One of the largest outstanding questions concerning the upper atmospheres of the giant planets is the energy crisis, wherein the observed low-latitude temperatures of these regions are hundreds of kelvin hotter than what the solar energy flux can provide (for example, ref. 28). The two main candidate resolutions to this crisis are equator-ward redistribution of auroral heating and the breaking of acoustic or gravity waves generated in the turbulent troposphere. Both of these potential solutions have challenges to overcome. According to some models[29], the movement of energy from the pole down to the equator is largely prohibited by the strong Coriolis forces generated by the large size and rapid rotation of these planets, and the effectiveness of gravity waves as a heat source remains largely unknown. Pole-to-pole observations of the upper atmosphere of Jupiter and Saturn[11,30] show that both have a temperature gradient that very gradually decreases from the pole to the equator, indicative of global transport of heat away from the auroral region. The somewhat higher temperatures seen at higher latitudes in this study are broadly consistent with this scenario.

At Saturn, momentum loading of the upper atmosphere, which could be driven by gravity waves, has been proposed as a mechanism that could reduce the efficacy of the Coriolis force in preventing the movement of heat from the pole down toward the equator[31]. The disturbances observed here are highly suggestive of gravity waves present in Jupiter's ionosphere. Having an upper atmosphere replete with these waves could similarly reduce the efficacy of Coriolis forces at Jupiter, enabling the equator-ward transport of heat, explaining the gradual pole-to-equator temperature gradient reported previously[11], suggestive of a global redistribution of auroral heating. In addition, the large-scale wave of elevated temperatures previously seen at the polar region[11] may also contribute to the wave activity seen at lower latitudes when it propagates towards the equator, although this was largely affecting the observed temperatures, not the densities, as is seen here. Although there is observational evidence of redistribution of auroral energy, reproducing these results with numerical modelling is very challenging, and the exact mechanism that allows heat to be redistributed is still an open question. By varying the incoming solar-wind pressure, and therefore the auroral heating, modelling has been able to show that some energy is able to move equator-ward[29], albeit only at levels of tens of kelvins.

The temperatures derived from the JWST data are relatively high, as expected from the 'energy crisis', but they are also very uniform across the field of view. Although heating has previously been observed above the GRS[13], no extreme temperatures were found in the present study. This potentially indicates that extreme GRS heating is time-variable or that upwelling from below can occasionally carve out the bottomside of the ionosphere[32], resulting in only high-altitude, high-temperature H_3^+ remaining. However, the presence of multiple interfering gravity waves in the JWST data may have important implications for ionospheric heating. Turbulence is present in the troposphere almost everywhere, so the breaking of gravity waves could produce localized heating at a large number of locations across the planet. As it stands, there is no modelling consensus to what degree gravity waves heat the upper atmosphere[33]. Further detailed modelling is required to determine the physical properties of the gravity waves responsible for shaping the low-latitude ionosphere: only certain combinations of wave parameters (for example, amplitude and wavelength) can explain the complex structures seen here, so these observations impose important constraints on future modelling efforts. Ultimately, by deriving those wave parameters based on observations such as these, better estimates of wave-induced heating can be made.

In the auroral region, the large-scale structure of H_3^+ emissions is governed by the interaction between the magnetosphere, ionosphere and atmosphere. However, it is possible that gravity waves would still provide small-scale ionospheric disturbances at high latitudes that are superimposed on the auroral emissions, so that the polar ionosphere is shaped by forcing both from above (magnetosphere) and from below (gravity waves generated in the troposphere). Overall, however, the polar ionosphere is predominantly shaped by magnetospheric processes, whereas the low-latitude ionosphere is driven largely by the coupling with the lower atmosphere. This highlights the importance of the ionosphere as an interface layer in a highly coupled neutral atmosphere–charged-particle ionosphere–magnetosphere system.

The fact that the lower and upper atmospheres are so strongly coupled at Jupiter may also imply strong coupling at other giant planets, with momentum transfer via gravity waves being an important mechanisms to shape the global ionosphere. Because these waves alter the ionospheric density, they also change the conductivity, which in turn will regulate the efficacy of any interaction with magnetospheric

currents, particularly at high latitudes. These JWST observations form the proof of concept for future investigations of this region: for example, if these ionospheric irregularities were monitored over time, the progression of these waves could be directly measured, providing a view of temporal variability and an opportunity to characterize the wave amplitudes and wavelengths.

Methods

The GRS of Jupiter was observed by JWST NIRSpec[34] on 27 July 2022 using the IFU and the F290LP/G329H grating/filter as part of ERS programme #1373: 'ERS Observations of the Jovian System as a Demonstration of JWST's Capabilities for Solar System Science' (Co-Principal Investigators: I. de Pater, T. Fouchet). The IFU produces a three-dimensional cube with two spatial dimensions covering 3″ × 3″ field of view, with each spaxel covering 0.1″ × 0.1″ and a third spectral dimension covering 2.87–4.01 μm (using the NRS1 detector only) at a spectral resolution, at wavelength λ, of $R = \frac{\lambda}{\Delta\lambda} \approx 2{,}700$. The NIRSpec IFU data was calibrated using the Python jwst calibration pipeline (v.1.9.5.dev3+g22acc46) up to Level 2 with Calibration References Data System context defined by jwst_1045.pmap. The MAST observation ID is jw01373-o005_t004_nirspec_g395h-f290lp. Geometry, for example latitude and longitude, was assigned to the data using the Python class JWSTSolarSystemPointing (https://github.com/JWSTGiantPlanets/NIRSPEC-Toolkit).

Six IFU mosaic tiles were acquired to capture the full extent of the GRS, illustrated in Fig. 1 with details listed in Table 1. Each tile is a single observation made up of 30 groups giving an effective exposure time of 322 s (5.4 min). The use of a large number of groups was specifically to capture the relatively weak H_3^+ emissions with a high signal-to-noise (S/N). Between 3.3 and 3.6 μm, the mean S/N is 55, whereas at 3.0 μm it is 274 (Fig. 2). The full 2 × 3 mosaic took a total of 53.0 min to complete, with a mean time separation of 3.9 min between each tile. Table 1 also lists the local time at the centre of each tile, showing that the prenoon to mid-afternoon sector was sampled. The maps in Fig. 1 and Fig. 4 were projected with a latitude and longitude resolution of 0.05°.

The Level 2 calibrated NIRSpec data contains a considerable amount of arc-like fringing, which appears to be especially apparent where the radiance is low, which is the case for the regions that contain emissions from H_3^+. To address this, a flat field was constructed from the six mosaic tiles, with the flat field of each wavelength bin being equal to the median of the six mosaic tiles. This works well when the spatial variability across the bin is small, for example for the H_3^+ bins, but does not work at all when there are bright discrete features, for example discrete cloud features at 3 μm. The flat-field procedure for a wavelength bin that contain strong H_3^+ emissions is illustrated in Supplementary Fig. 4. Ultimately, the process used to remove the fringing does clearly improve the fidelity of the data and does not introduce any significant artificial features in the resulting maps.

Figure 2a shows a model H_3^+ spectrum generated using h3ppy with parameters broadly appropriate for Jupiter's low-latitude ionosphere (temperature $T = 700$ K, column density $N = 5 \times 10^{15}$ m^{-2} (ref. 11). Figure 2b shows the full NRS1 spectra from both outside and inside the GRS (points P_1 and P_2 in Fig. 1). A significant number of H_3^+ lines are available in this wavelength range, but disentangling weak lines from a very bright background is extremely difficult. However, between 3.2 and 3.6 μm there is significant absorption of sunlight by CH_4 in the troposphere and stratosphere, rendering this region very dark (indicated as grey in Fig. 2b and shown in Fig. 3a). Within this band, there are two dominant spectral features: (1) non-LTE solar excited CH_4 emission contained within 3.2 and 3.4 μm and (2) discrete emission lines from H_3^+. To isolate the H_3^+ spectrum, the solar excited CH_4 spectrum needs to be subtracted. The full radiative transfer modelling required to model the full CH_4 spectrum[5] is outside the scope of this study, and a simplified, yet effective, approach is adopted here. The spectral shape of the non-LTE CH_4 emissions can be approximated by modelling two separate LTE components: the fundamental transitions ($\nu_3 \rightarrow$ ground) and the hot-band transitions ($\nu_3 + \nu_4 \rightarrow \nu_4$). Using the HITRAN[35] CH_4 line list, the radiance of the two components can be modelled separately at a fixed temperature (300 K), as well as a third-order polynomial background, which works well over limited wavelength ranges. Here, we use four separate narrow wavelength windows for the CH_4 fitting: (1) 3.23–3.31 μm, (2) 3.37–3.40 μm, (3) 3.40–3.43 μm and (4) 3.528–3.56 μm. An example CH_4 model fit for point P_2 is shown in Fig. 3b. The morphology of the integrated CH_4 radiance can be seen in Supplementary Fig. 1. The residual between the NIRSpec data and the CH_4 model then contains the H_3^+ spectrum (for example, Fig. 3c), which is then fitted with h3ppy. The fitting program implements the H_3^+ line list of ref. 36 and the partition function of ref. 37.

The analysis sequence illustrated in Fig. 3 was repeated for all IFU spaxels in this dataset, generating 6,927 individual H_3^+ spectral fits. Note that this is larger than the nominal 5,400 number of spaxels contained within six NIRSpec IFU observations and is due to the fact that the JWST pipeline drizzles the cubes onto a grid that is slightly larger than the 30 × 30 spaxel IFU when using the ifualign coordinate system.

The magnetic field modelling and field-line tracing for Fig. 1 were performed using the JupiterMag model[38], using the latest magnetic field model derived from the Juno magnetometer observations from 33 perijoves of the primary mission[9].

For a broader context, Supplementary Fig. 5 shows the magnetic field strength and the smoothed temperature distribution derived from the data, and Supplementary Fig. 6 shows the wavelength-integrated H_3^+ total emissions[37] on top of the H_3^+ imaging observations of ref. 4. Supplementary Fig. 2 shows the unprojected integrated H_3^+ radiance and the correlation between the temperature and H_3^+ density for tiles (i)–(v).

Supplementary Fig. 7 cuts along −18° latitude and 291°W longitude of the H_3^+ radiance, temperature and column density, emphasizing that the radiance features are largely driven by column density, not by temperature. The small-scale features are clearly seen, with large variability present within these profiles.

The gaussian filter applied to Fig. 4 and Supplementary Figs. 5 and 6 is the ndimage.gaussian_filter function available in scipy.

The JWST ERS Jupiter programme also included both NIRSpec FL170P/G235H filter/grating and MIRI Channel 1 Short observations of the GRS, both capturing a number of H_3^+ emission lines at ~2 μm and ~5 μm, respectively. These could have provided a means through which to examine the longer-term spatial variability of the ionospheric features, because they were obtained at different epochs. However, the large magnitude and intricate structure of the underlying signal (deep thermal emissions and aerosol scattering) and the low S/N of the H_3^+ emission lines renders this mapping impossible. Only the NIRSpec FL290LP/G395H filter/grating was optimized for the relatively weak H_3^+ emissions and used an effective exposure time roughly ten times longer than the other settings.

Data availability

JWST data used in this study were obtained from the Mikulski Archive for Space Telescopes at the Space Telescope Science Institute (https://archive.stsci.edu/), which is operated by the Association of Universities for Research in Astronomy, Inc., under NASA contract NAS 5-03127 for the JWST. JWST NIRSpec ERS #1373 observations of Jupiter's GRS used here are available via MAST at https://doi.org/10.17909/yedm-f607.

Code availability

The open source Python H_3^+ fitting code h3ppy is available at https://github.com/henrikmelin/h3ppy. The JupiterMag field-line tracing code is available at https://github.com/mattkjames7/JupiterMag. All remaining code used for this analysis of the JWST data can be found at https://github.com/henrikmelin/jupiter-grs-h3p.

References

1. de Pater, I. et al. JWST observations of the Jovian system from commissioning and ERS data. *AAS/DPS Meeting Abstracts* **54**, 306.07 (2022).
2. Grodent, D., Waite, J. H. & Gérard, J. C. A self-consistent model of the Jovian auroral thermal structure. *J. Geophys. Res.* **106**, 12933–12952 (2001).
3. Stallard, T. S. et al. Cassini VIMS observations of H_3^+ emission on the nightside of Jupiter. *J. Geophys. Res. Space Phys.* **120**, 6948–6973 (2015).
4. Stallard, T. S. et al. Identification of Jupiter's magnetic equator through H_3^+ ionospheric emission. *Nat. Astron.* **2**, 773–777 (2018).
5. Sánchez-López, A. et al. The CH_4 abundance in Jupiter's upper atmosphere. *Astron. Astrophys.* **662**, A91 (2022).
6. Miller, S. et al. Mid-to-low latitude H_3^+ emission from Jupiter. *Icarus* **130**, 57–67 (1997).
7. Anguiano-Arteaga, A., Pérez-Hoyos, S., Sánchez-Lavega, A., Sanz-Requena, J. F. & Irwin, P. G. Vertical distribution of aerosols and hazes over Jupiter's Great Red Spot and its surroundings in 2016 from HST/WFC3 imaging. *J. Geophys. Res. Planets* **126**, e2021JE006996 (2021).
8. Drossart, P. H_3^+ as an ionospheric sounder of Jupiter and giant planets: an observational perspective. *Philos. Trans. R. Soc. Lond. A* **377**, 20180404 (2019).
9. Connerney, J. E. P. et al. A new model of Jupiter's magnetic field at the completion of Juno's prime mission. *J. Geophys. Res. Planets* **127**, e2021JE007055 (2022).
10. Lam, H. A. et al. A baseline spectroscopic study of the infrared auroras of Jupiter. *Icarus* **127**, 379–393 (1997).
11. O'Donoghue, J. et al. Global upper-atmospheric heating on Jupiter by the polar aurorae. *Nature* **596**, 54–57 (2021).
12. Fletcher, L. N. et al. Thermal structure and composition of Jupiter's Great Red Spot from high-resolution thermal imaging. *Icarus* **208**, 306–328 (2010).
13. O'Donoghue, J., Moore, L., Stallard, T. S. & Melin, H. Heating of Jupiter's upper atmosphere above the Great Red Spot. *Nature* **536**, 190–192 (2016).
14. Melin, H. et al. On the anticorrelation between H_3^+ temperature and density in giant planet ionospheres. *Mon. Not. R. Astron. Soc.* **438**, 1611–1617 (2014).
15. Adriani, A. et al. Preliminary JIRAM results from Juno polar observations: 2. Analysis of the Jupiter southern H_3^+ emissions and comparison with the north aurora. *Geophys. Res. Lett.* **44**, 4633–4640 (2017).
16. Miller, S., Stallard, T. S., Tennyson, J. & Melin, H. Cooling by H_3^+ emission. *J. Phys. Chem. A* **117**, 9770–9777 (2013).
17. Johnson, R. E. et al. Mapping H_3^+ temperatures in Jupiter's northern auroral ionosphere using VLT-CRIRES. *J. Geophys. Res. Space Phys.* **123**, 5990–6008 (2018).
18. Valek, P. W. et al. Juno in situ observations above the Jovian equatorial ionosphere. *Geophys. Res. Lett.* **47**, e2020GL087623 (2020).
19. Schunk, R. & Nagy, A. *Ionospheres: Physics, Plasma Physics, and Chemistry* (Cambridge Univ. Press, 2009).
20. Hueso, R., Sánchez-Lavega, A. & Guillot, T. A model for large-scale convective storms in Jupiter. *J. Geophys. Res. Planets* **107**, 5075 (2002).
21. Barrow, D., Matcheva, K. I. & Drossart, P. Prospects for observing atmospheric gravity waves in Jupiter's thermosphere using H_3^+ emission. *Icarus* **219**, 77–85 (2012).
22. Sánchez-Lavega, A. et al. The rich dynamics of Jupiter's Great Red Spot from JunoCam: Juno images. *Astron. J.* **156**, 162–171 (2018).
23. Makela, J. J. A review of imaging low-latitude ionospheric irregularity processes. *J. Atmos. Terr. Phys.* **68**, 1441–1458 (2006).
24. Achilleos, N. et al. JIM: a time-dependent, three-dimensional model of Jupiter's thermosphere and ionosphere. *J. Geophys. Res.* **103**, 20089–20112 (1998).
25. Nakamura, Y. et al. Effect of meteoric ions on ionospheric conductance at Jupiter. *J. Geophys. Res. Space Phys.* **127**, e2022JA030312 (2022).
26. Seiff, A. et al. Thermal structure of Jupiter's upper atmosphere derived from the Galileo probe. *Science* **276**, 102–104 (1997).
27. Waite, J. H. et al. Equatorial X-ray emissions: implications for Jupiter's high exospheric temperatures. *Science* **276**, 104–108 (1997).
28. Strobel, D. F. & Smith, G. R. On the temperature of the Jovian thermosphere. *J. Atmos. Sci.* **30**, 718–725 (1973).
29. Yates, J. N., Achilleos, N. & Guio, P. Response of the Jovian thermosphere to a transient 'pulse' in solar wind pressure. *Planet. Space Sci.* **91**, 27–44 (2014).
30. Brown, Z. et al. A pole-to-pole pressure-temperature map of Saturn's thermosphere from Cassini Grand Finale data. *Nat. Astron.* **4**, 872–879 (2020).
31. Müller-Wodarg, I. C. F. et al. Atmospheric waves and their possible effect on the thermal structure of Saturn's thermosphere. *Geophys. Res. Lett.* **46**, 2372–2380 (2019).
32. Conrath, B. J., Flasar, F. M., Pirraglia, J. A., Gierasch, P. J. & Hunt, G. E. Thermal structure and dynamics of the Jovian atmosphere 2. Visible cloud features. *J. Geophys. Res.* **86**, 8769–8775 (1981).
33. Yelle, R. V. & Miller, S. in *Jupiter: The Planet, Satellites and Magnetosphere* (eds Bagenal, F. et al.) Ch. 9 (Cambridge Univ. Press, 2004).
34. Jakobsen, P. et al. The Near-Infrared Spectrograph (NIRSpec) on the James Webb Space Telescope. I. Overview of the instrument and its capabilities. *Astron. Astrophys.* **661**, A80 (2022).
35. Gordon, I. E. et al. The HITRAN2016 molecular spectroscopic database. *J. Quant. Spectrosc. Radiat. Transf.* **203**, 3–69 (2017).
36. Neale, L., Miller, S. & Tennyson, J. Spectroscopic properties of the H_3^+ molecule: a new calculated line list. *Astrophys. J.* **464**, 516 (1996).
37. Miller, S., Stallard, T. S., Melin, H. & Tennyson, J. H_3^+ cooling in planetary atmospheres. *Faraday Discuss.* **147**, 283–291 (2010).
38. Wilson, R. J. et al. Internal and external Jovian magnetic fields: community code to serve the magnetospheres of the outer planets community. *Space Sci. Rev.* **219**, 15 (2023).

Acknowledgements

H.M. was supported by the STFC James Webb Fellowship (ST/W001527/1) at the University of Leicester, UK. J.O'D. was supported by the STFC Ernest Rutherford Fellowship ST/X003426/1 at the University of Reading. I.d.P., P.M.F., M.R.S. and M.H.W. are in part supported by the Space Telescope Science Institute grant no. JWST-ERS-01373. T.S.S. was supported by an STFC Consolidated Grant (ST/Y005325/1) at the Northumbria University, UK. L.M. acknowledges support by NASA grant no. 80NSSC20K1045 issued through the Solar System Workings Program. L.N.F. was supported by a European Research Council Consolidator Grant under the European Union's Horizon 2020 research and innovation program, grant agreement 723890 at the University of Leicester. R.H. and A.S.L. were supported by grant no. PID2019-109467GB-I00 funded by MCIN/AEI/10.13039/501100011033/ and were also supported by Grupos Gobierno Vasco IT1742-22. K.L.K. was supported by a Northumbria University Research Studentship. P.I.T., J.H. and E.M.T. were supported by STFC studentships at the University of Leicester. G.S.O. was supported at the Jet Propulsion Laboratory, California Institute of Technology, under a contract with the National Aeronautics and Space Administration (80NM0018D0004). For the purpose of open access, the authors have applied a creative commons attribution (CC BY) licence to any author-accepted manuscript version arising.

Author contributions

H.M. led the project, performed the data analysis, devised the fitting procedures and wrote the manuscript. J.O'D., L.M., T.S.S., P.I.T., E.T. and R.W. provided context and contributed to the interpretation of the H_3^+ emissions. L.N.F., R.H., A.S.L. and G.S.O. provided the context for the troposphere and stratosphere. K.K. provided the low-latitude observations of ref. 4. M.T.R., J.H. and O.R.T.K. worked on the post-pipeline reduction of the NIRSpec IFU data. M.W., K.d.K., E.L., A.M. and M.R.S. designed and planned the observations. I.d.P. and T.F. led the Jupiter ERS programme. P.F. provided validation of the NIRSpec flux calibration. R.H. provided guidance on the JWST Near Infrared Camera observations. B.H. helped with the JWST calibration pipeline. M.K.J. developed the JupiterMag tool to model Jupiter's magnetic field and perform field-line tracing. All authors reviewed and edited the paper.

Competing interests

The authors declare no competing interests.

Additional information

Supplementary information The online version contains supplementary material available at https://doi.org/10.1038/s41550-024-02305-9.

Correspondence and requests for materials should be addressed to Henrik Melin.

Peer review information *Nature Astronomy* thanks Pierre Drossart, Robert Ebert and the other, anonymous, reviewer(s) for their contribution to the peer review of this work.